Sustainable Materials and Technologies 48 (2026) e01955

Contents lists available at ScienceDirect

Sustainable Materials and Technologies

journal homepage: www.elsevier.com/locate/susmat

Polymer-containing dolostone-matrix composites for room-temperature thermal energy storage by cold sintering

Dovilė Škarnulytė [a,b], Levent Karacasulu [a,*], Emanuela Callone [a], Sereno Sacchet [a,c], Luca Fambri [a,c], Meriem Bembli [a], Mauro Bortolotti [a], Paolo Bettotti [d], Jonathan Selorm Degbedzui [a], Giulia Fredi [a,c], Sandra Dirè [a], Mattia Biesuz [a,c,*]

[a] University of Trento, Department of Industrial Engineering, Via Sommarive 9, 38123 Trento, Italy
[b] Vilnius University, Institute of Chemistry, Naugarduko 24, LT-03225 Vilnius, Lithuania
[c] INSTM, Via Giuseppe Giusti, 9, 50121 Firenze, Italy
[d] University of Trento, Department of Physics, Via Sommarive 14, 38123 Trento, Italy

ARTICLE INFO

Keywords:
Cold sintering process
Dolostone
Ceramic matrix composites
Thermal energy storage

ABSTRACT

The cold sintering process (CSP) was employed at room temperature to consolidate dolostone powders and dolostone-matrix composites containing a dispersed organic phase for near-room temperature thermal energy storage. The materials' microstructure and structure were thoroughly analyzed, and their mechanical and thermal properties were assessed. The results show that the composite's density increases with CSP pressure and bending strength (up to about 10–12 MPa). These composites exhibit a thermal energy storage capacity of approximately 15 J g^{-1} at near-room temperature, thanks to the latent heat of fusion/crystallization of the organic phase (i.e., the phase change material, PCM). Specific care needs to be taken in choosing the PCM, as it could cause unwanted interactions with the CSP solution. The developed process offers a new approach for manufacturing sustainable materials with low embodied energy and thermal management capabilities.

1. Introduction

The building sector is responsible for approximately 40% of global raw material extraction and energy consumption [1–3]. Consequently, sustainable development policies aligned with the *UN 2030 Agenda* must prioritize innovations in this industry. The carbon footprint of building materials arises from multiple processes—including mineral mining, transportation, milling, and drying [4]— but the most energy-intensive step remains the thermal treatment of clays, carbonates, quartz, and feldspars for producing mortars, cement, and ceramics. Specifically, the firing process alone accounts for nearly two-thirds of the energy consumption in the ceramic industry.

In the past decade, several non-conventional firing processes have been developed to reduce firing time or temperature [5–7]. Among these, the cold sintering process (CSP) [8–12] shows the greatest potential for reducing energy consumption associated with firing (a reduction of 90% or more).

Inspired by the natural lithification of sedimentary rocks [9,10], CSP applies external pressures of a few hundred MPa while a small amount of liquid phase is present in the sample (often a water solution). The external pressure enhances the driving force for densification beyond the sole curvature effect, while the liquid phase provides a fast avenue for ion diffusion. As such, unlike traditional ceramic manufacturing, CSP operates at temperatures below 350 °C—significantly lower than the conventional firing range of 900–1250 °C [12–15].

Since its development in 2016 at Penn State University [16], the research on CSP has primarily focused on functional ceramics (piezoelectrics, ferroelectrics, and thermoelectrics…). In fact, it enables the consolidation of metastable phases, unconventional microstructural tailoring, ceramics/metal, and organic/inorganic compound integration [17–24]. Interestingly, CSP can also be used to obtain transparent ceramics for optical applications [25], and allow the production of advanced composites, including metastable inorganic compounds [26,27]. However, the environmental benefits of CSP for these materials are relatively modest, due to their low production volumes. Applying CSP to high-volume construction materials could yield far greater environmental benefits.

Currently, only a limited number of studies address the CSP of

* Corresponding authors at: University of Trento, Department of Industrial Engineering, Via Sommarive 9, 38123 Trento, Italy.
E-mail address: mattia.biesuz@unitn.it (M. Biesuz).

https://doi.org/10.1016/j.susmat.2026.e01955
Received 6 December 2025; Received in revised form 9 February 2026; Accepted 9 March 2026
Available online 10 March 2026

building materials, including calcium carbonate [25–29], construction and demolition wastes [28–30], diatomites [31], geopolymers [32–34], sand-gypsum [35] and sand-evaporite composites [36]. Specifically, CSP research on carbonates has focused on highly reactive powders (e.g., vaterite, mixtures of aragonite/calcite, hydromagnesite…) to facilitate consolidation. Still, not much is known about the CSP parameters – microstructure – properties relation in industrial minerals based on natural carbonates.

An additional opportunity arises from CSP's capacity for organic/inorganic integration—an outcome that has been particularly relevant in functional ceramics but could have far-reaching implications in the building sector. In fact, organic compounds with a melting point close to room temperature can effectively act as thermal energy storage systems [37] absorbing latent heat when the temperature exceeds its melting point and releases it when the temperature falls below. These have been, therefore, studied as passive cooling/heating systems in buildings [38–40].

Such materials, able to store and release enthalpy through a phase transition, are called phase change materials (PCMs). The PCMs selection is based on their melting point, around which the temperature can be stabilized. In building applications, organic PCMs are generally used as they possess a melting point close to room temperature. Indeed, the PCMs could be incorporated in architectural elements to introduce some thermal energy storage ability and improve the energy efficiency of the building [41]. Generally, this is achieved by incorporating the PCMs in a setting matrix (cement, plaster, geopolymers… [42–51]. The PCMs, once in the molten state, need to be confined to avoid its leakage, which has been done through the use of organic or inorganic microcapsules [52–54], or through the use of mineral porous stabilizers [52].

In this study, we explore the applicability of CSP to an industrial raw material (milled dolostone) to obtain composites with organic compounds possessing a melting point near room temperature. This work provides the first proof-of-concept demonstration of using CSP as a tool to embed phase change materials with thermal energy storage capability within a multifunctional ceramic-matrix composite.

2. Experimental procedures

2.1. Materials and sample preparation

Dolostone was mined from natural sedimentary rocks in Val di Non (Trentino, Italy) by the company Tassullo. The mineral was milled using alumina spheres in a polyethylene jar for 24 h using a Turbula 3D-mixer. The milling process was carried out in a deionized water medium with a 1:1 mass ratio between dolomite and the solvent. After milling, the powder possessed a d_{50} of 0.4 μm and d_{90} of 0.7 μm (determined by dynamic light scattering, Anton-Paar Litesizer DLS 500, Fig. 1). The theoretical density was determined by the He pycnometry (Ultrapyc5000, Anton Paar), and resulted 2.83 g cm^{-3} with a relative error of 0.15%.

Two different types of expanded graphite-stabilized PCM (EGS-PCM) were tested and produced following the procedures reported in a previous work [55]. Herein, the addition of graphite to the PCM is needed to stabilize its shape and avoid PCM leakage when it reaches the liquid state. Fatty acids (Carlo Erba, palmitic acid ≥50 wt% and stearic acid ≥40 wt%) and paraffin (Rubitherm® RT28HC) were employed as PCMs; the former possess a melting point of about 55 °C, while the latter melts at 28 °C. The graphite was purchased from SGL Carbon with a tap density of 25 g l^{-1}. The mass ratio between expanded graphite (EG) and PCM was 9:1. In the following, we will name the two EGS-PCMs Gr28 and Gr55, the number referring to their melting point.

A 2 M H_3PO_4 solution was prepared by mixing DI water and phosphoric acid (85%, purchased from Sigma Aldrich). Then, 70 μL of the said solution was added to a powder mixture consisting of 90 wt% dolomite and 10 wt% EGS-PCM. The weight of the powder mixture was ≈ 600 mg. Some samples containing only dolostone (i.e., without any organics) were prepared for comparison. Preliminary tests were conducted with 1 M solutions, which provided density data similar to or even better than those of 2 M; however, the mechanical properties evaluated by equibiaxial bending were substantially lower. Therefore, the work focused solely on the 2 M solution. The resulting mixture was thoroughly ground in an agate mortar, transferred into a die, and subjected to uniaxial pressing at pressures of 100, 200, 300, 400, and 500 MPa for 15 min. The resulting pellets were removed from the die and allowed to dry at room temperature. A summary of the sample preparation procedure is sketched in Fig. 1a along with a picture of the cold-sintered materials (Fig. 1c). Room temperature cold sintering and drying were selected to reduce the risk of evaporation decomposition of the PCM during processing.

The samples will be labelled as CSP-D, CSP-D/28, and CSP-D/55 for cold-sintered dolostone, dolostone+Gr28, and dolostone+Gr55, respectively.

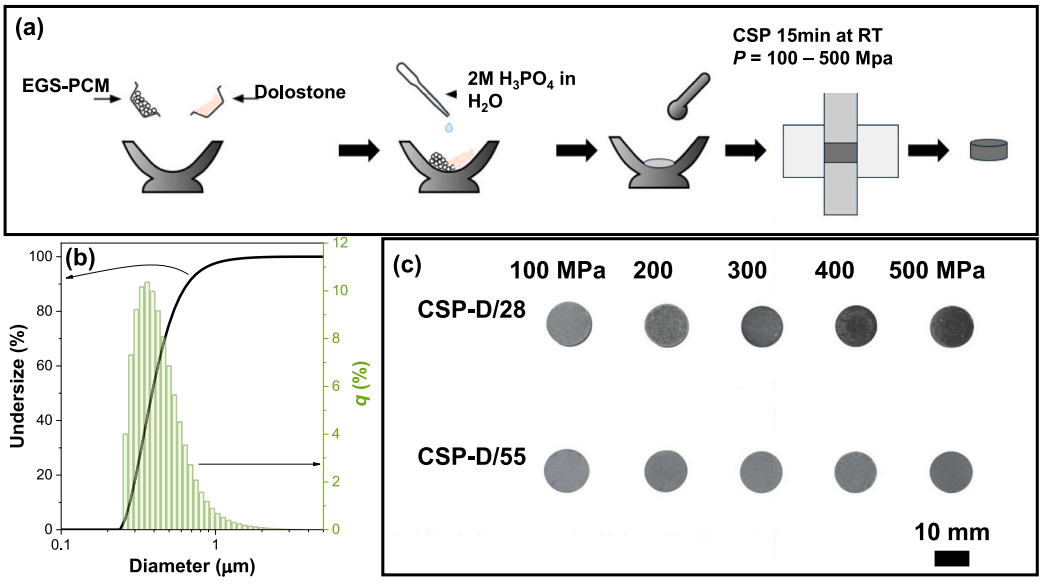

Fig. 1. Schematic representation of the processing step to manufacture dolostone/PCM composites; (b) dolostone particle size distributions after the milling process; (c) a picture of the cold-sintered composites.

2.2. Characterization

The bulk density of the sample was determined by the geometrical method using a caliper with a sensitivity of 0.01 mm and an analytical balance (±0.1 mg). The density was evaluated after the drying process was completed. FEG-SEM micrographs were obtained using a Zeiss Supra40 microscope on fresh fracture surfaces. Before the analysis, the samples were coated with a thin Pt-Pd layer obtained by sputtering.

The mechanical properties were evaluated by the piston-on-three-ball method (equibiaxial flexion) using an MTS 810 equipped with a 100 kN load cell and using the ISO 6872:15 standard as a reference. The sample was placed on three supporting balls, equally spaced at 120°, and loaded by WC-Co piston (2 mm). The strength was calculated according to the equations in [56].

The density and mechanical strength data are reported as averages with the error bar corresponding to the standard deviation of the measurements carried out on 4 samples for the intermediate pressures (2000, 300, and 400 MPa) and on 6 samples for the end-member pressures (100 and 500 MPa).

Crystallographic phase identification was performed by means of powder X-Ray diffraction (IPD3000, Italstructures) using a Cu anode source coupled to parallel multilayer optics (Axo Dresden GmbH). Powder patterns were collected in reflection geometry by means of a multichannel silicon strip detector (Dectris Mythen) over a 10–110° 2θ range (0.02° step size) in continuous scan mode (30 min total acquisition time).

Fourier transform infrared (FTIR) spectra were recorded in transmission mode with a Nicolet Apex spectrometer using KBr pellets in the range 4000–400 cm^{-1}, with 4 cm^{-1} resolution.

^{1}H, ^{13}C, and ^{31}P magic angle spinning nuclear magnetic resonance (MAS NMR) analyses were carried out with a Bruker 400WB instrument equipped with a CPMAS probe. NMR spectra were acquired with cross-polarized (CP) or single (SP) pulse sequences. Used parameters: ^{1}H frequency 400.13 MHz, $\pi/2$ 4.5 ms, recycle delay 3 s, 32 scans;^{13}C frequency 100.69 MHz, $\pi/6$ 3.75 ms, recycle delay 100 s, 128 scans, for CP 1.5 ms of contact time, recycle delay 3 ms and 1 k scans;^{31}P frequency 161.99 MHz, $\pi/4$ 3.5 ms, recycle delay 150 s, 32 scans. Samples were packed in 4 mm zirconia rotors, which were spun at 7 or 10 kHz under air flow. The line-shape fitting was performed using Lorentzian components with Bruker Topspin 3.6 software, and it was considered acceptable at 95% confidence level.

Differential scanning calorimetry (DSC) tests were performed using a Mettler DSC5+ facility (Mettler-Toledo, Greifensee, Switzerland) equipped with Al crucibles. The tests were performed under a nitrogen flow of 100 cm^3 min^{-1} between 20 and 80 °C with a rate of 10 °C min^{-1}.

Additionally, two tests were performed to assess the thermal stability of the prepared composites. First, a leakage test was operated for 1 week at 35 °C and 65 °C on the samples CSP-D/28 and CSP-D/65 sintered under 500 MPa, respectively. After the leakage test, the CSP-D/28 sample underwent cyclic DSC tests (100 heating-cooling cycles), which were performed with the same DSC equipment described above. The DSC cycle was operated at 20 °C min^{-1} between −10 °C and 50 °C. Thermal diffusivity was determined from 5 °C to 75 °C by laser flash analysis (LFA) using an LFA 446 (Netzsch GmbH.). The data were interpolated with the standard materials model. The flash signal was obtained using a 250 V pulse possessing a width of 0.6 ms. At 15 °C, the specific heat capacity was determined for comparison with a pyroceram 9606 reference characterized by a density of 2.59 g cm^{-3} and a thickness of 2.5 mm.

Infrared (IR) thermography was performed using an IRtech Fotric 348 A (Fotric), acquiring a frame every 30 s. The mean temperature of the square traced with the software was reported as a function of time. The thermal evolution of the samples was evaluated within a climatic chamber DM340C by Angelantoni Industrie S.r.l. operating heating and cooling ramps at 1 °C min^{-1}. The thermal cycle was operated between 5 and 40 °C.

3. Results

Fig. 2a reports the density evolution during CSP as a function of the material composition and external pressure. The data show substantial densification as the pressure increases for both the composites, including Gr55 and Gr28 compounds. The density evolution with pressure is indeed substantial, with a relative density increase of about 10–15% when the pressure rises from 100 to 500 MPa, reaching peak values exceeding 80%. The densification upon CSP is affected by the type of added EGS-PCM, the density of composite CSP-D/55 being always lower than CSP-D/28. On the other hand, the dolostone samples not containing any PCM are clearly less dense than the composites.

SEM micrographs on the fresh fracture surface of CSP-D material show a porous structure (Fig. 2b), consistent with the density data, with some development of interparticle necking and densification. Densification is mostly visible in the regions where small sub-micrometric particles are present, as evidenced by the inset in Fig. 2b. When considering the CSP-D/28 composites, the fracture surface clearly evidences the presence of isolated regions with a flattened geometry that can be attributed to the Gr28 compound (Fig. 3c,d). This appears oriented orthogonally to the CSP load, with the orientation increasing with the pressure. The Gr28 is embedded in a dolomite matrix possessing a microstructure similar to that of the CSP-D sample (Fig. 2e).

The microstructure of CSP-D/55 composition shows a strong evolution with the CSP pressure. When the pressure is low (i.e., 100 MPa), we can differentiate regions with different levels of densification (Fig. 2f,g,h). When the pressure increases, the “low density areas” detectable under 100 MPa disappear while regions with a darker contrast form (Fig. 2i). The dark regions appear to possess a surface texture similar to the dolostone powder (Fig. 2l,m), which is, however, covered by a secondary phase (likely a residue from the Gr55 compound).

The FTIR spectra and XRD patterns of the milled dolostone show coherent features ascribed to the carbonates (Fig. 3). These are signaled by the main diffraction features of dolomite (mixed Ca-Mg carbonate, ICDD 360426) and minor reflection associated with calcite (ICDD 721650) (Fig. 3a). The key vibrational features of carbonate ions can be easily detected (Fig. 3b): at 1445 cm^{-1} the strong asymmetric stretching of the carbonate ion (ν_3 CO_3^{2-}), 877 cm^{-1} the out-of-plane bending vibration of CO_3^{2-} (ν_2), and at 719 cm^{-1} the in-plane bending vibration of CO_3^{2-} (ν_4) [57]. The dolostone appears nearly unchanged after the cold sintering treatment, both in terms of vibrational and diffraction features.

The FTIR spectra of the two EGS-PCM materials (Fig. 3b) show the characteristic band of the organic compounds: overlapped bands in the 2960–2840 cm^{-1} range due to C-H stretching vibrations from aliphatic chains, and two sharp peaks at 1471 and 1383 cm^{-1} due to the CH_2 and CH_3 bending modes of the hydrocarbon chain, confirming the incorporation of paraffin/fatty acids in the graphite matrix [58,59]. Moreover, Gr55 exhibits another distinct band at 1702 cm^{-1}, corresponding to the C=O stretching of carboxylic acids, confirming the presence of stearic and palmitic acid components. The crystalline nature of the two EGS-PCMs is further confirmed by the powder diffraction patterns, highlighting diffraction peaks corresponding to pure n-Octadecane (CSD entry NOCTDC) for Gr28 and a mixture of stearic and palmitic acid (CSD entries STARAC and YEFWEM) in the case of Gr55 (Fig. 3a).

The FTIR spectra and XRD patterns of the composite materials show the overlapping of dolostone and EGS-PCM characteristic features. However, the carbonyl stretching vibration is very weak in the CSP-D/55-500 MPa sample, suggesting the loss of part of the carboxylic acids during CSP. The loss of the PCM in this material is confirmed by the weak diffraction features associated with the stearic/palmitic acid (PCM55); actually, in the CSP-D/55-500 MPa composite, only the main diffraction peak of the PCM can be detected at $2\theta \approx 21°$. On the other hand, the diffraction features of the paraffin (PCM28) are fully recognizable in the composite (CSP-D/28-500 MPa).

Finally, a slight increase of the broad small double band at 1080 and 1031 cm^{-1} could be tentatively attributed to the ν_3 stretching of PO_4^{3-}

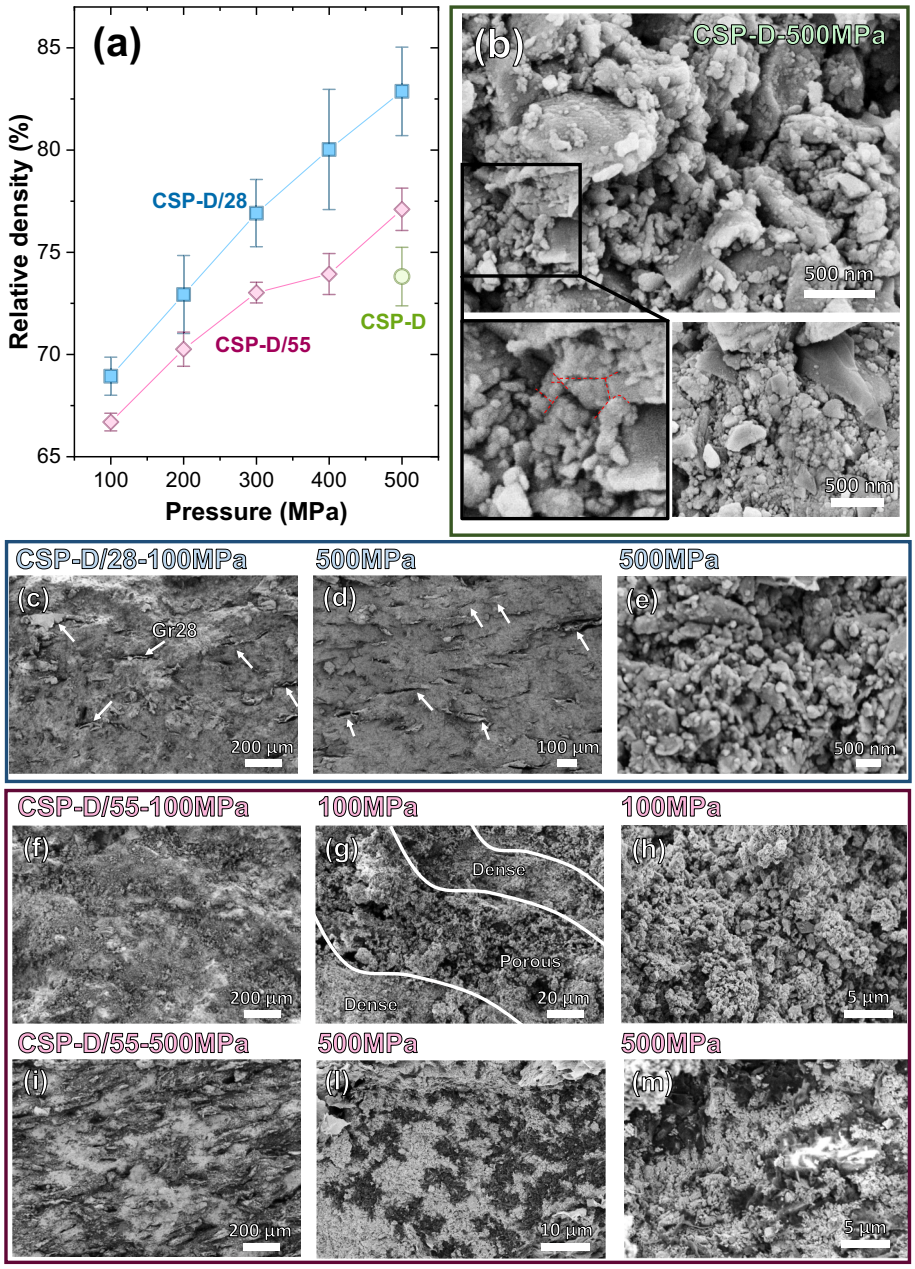

Fig. 2. (a) Relative density of cold-sintered dolostone and dolostone-matrix composites as a function of the CSP pressure. SEM micrographs of the fresh fracture surface of (b) dolostone cold sintered under 500 MPa, the red dash and dot lines evidence the formation of interparticle necking; (c,d) low-mag micrographs of composites with Gr28 compound (highlighted with white arrows) and (e) magnification of the dolostone matrix; (f,g) low-mag micrographs of composites with Gr55 produced under 100 MPa evidencing heterogeneous microstructure and (h) magnification of a low-density region; (i,l,m) micrographs at different magnifications of the composites containing Gr55 and cold sintered under 500 MPa.

[60–62] introduced with the CSP solution.

Fig. 4a shows the ^{13}C MAS NMR spectra of the samples. The ^{13}C spectrum of dolostone is characterized by a single sharp resonance at 170.8 ppm with a full width at half-maximum (FWHM) of 72 Hz [63]. The lineshape is not completely symmetric, displaying a small right shoulder. This indicates slightly different configurations of the carbon site, possibly due to crystal disorder or the presence of a very small number of Ca-rich domains in proximity to protons, as supported by the calcite peaks detected by XRD [64]. The spectral features of this signal are sensitive to the presence of paramagnetic elements within the crystal lattice, since the ^{13}C spin-lattice relaxation rate influences the signal intensity. They are also affected by the substitution of Ca or Mg with other elements, which can lead to small shifts or broadening of the resonance [65]. Cold sintering does not appear to alter this configuration, since both the chemical shift (170.8 ppm, with right shoulder) and the linewidth (68 Hz) remain essentially unchanged.

In contrast, the composite materials with Gr28 and Gr50 PCM show a downfield shift of the main resonance to 170.0 ppm, an asymmetric line shape with a component at 167.7 ppm, and a significantly broader FWHM of 204 and 197 Hz, respectively. This behavior could be attributed to a detrimental effect of graphite on the NMR signals. The presence of graphite is confirmed by the extremely broad resonance at the noise level, centered around 100 ppm.

In addition, the CSP-D/28-500 MPa sample shows a peak at about 32 ppm, which can be assigned to the aliphatic chains of paraffin (^{13}C MAS spectrum). The corresponding PCM peak is not observed in the CSP-D/55-500 MPa sample, possibly due to a lower PCM loading, which is consistent with the XRD and FTIR results.

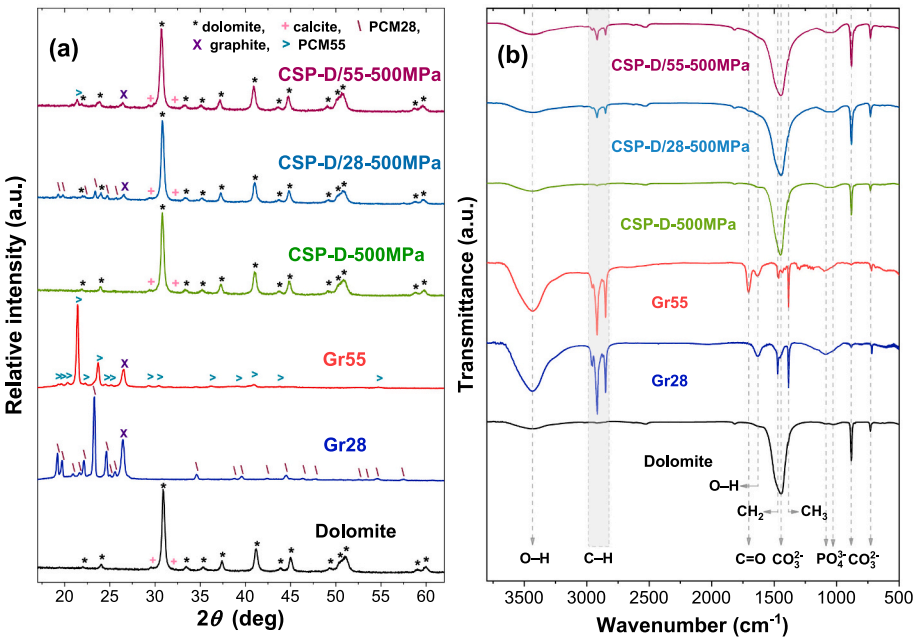

Fig. 3. (a) XRD patterns and (b) FTIR spectra of the pristine dolostone, the two EGS-PCMs, and cold sintered materials under 500 MPa.

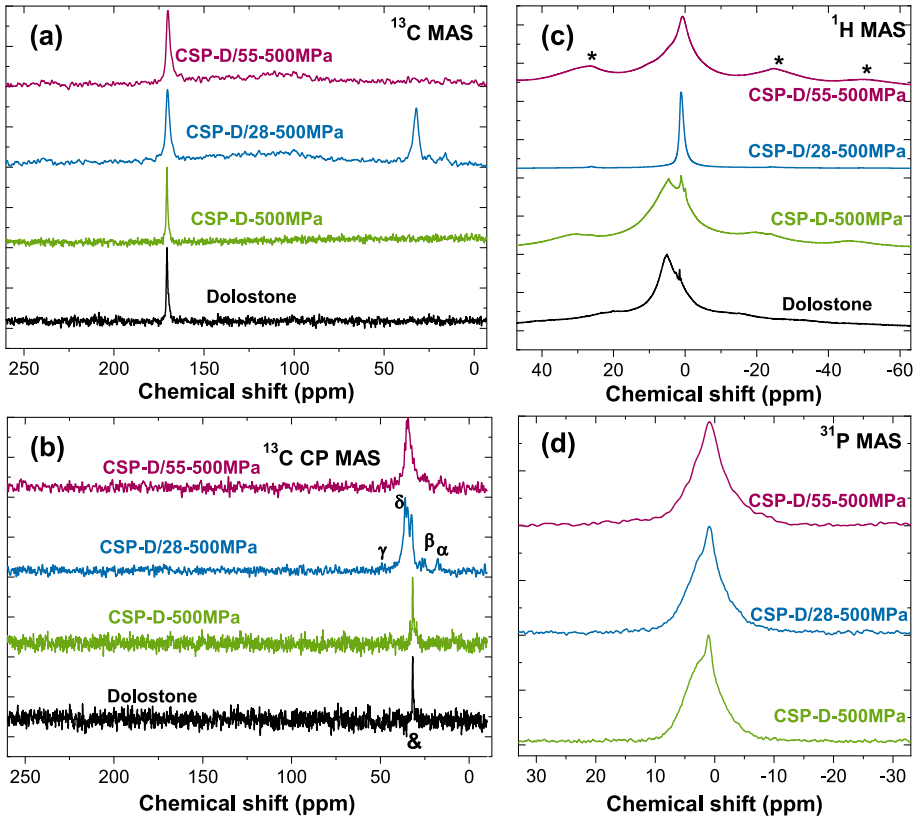

Fig. 4. (a) ^{13}C MAS and (b) CP MAS, (c) ^{1}H MAS, and (d) ^{31}P MAS NMR spectra of the pristine dolostone and cold sintered materials under 500 MPa. Note that the NMR analysis of the EGS-PCM alone was not possible due to the large amount of conductive graphite phase in the material. In the ^{1}H MAS spectrum, " * " highlights the sidebands, while in the ^{13}C CP MAS "&" highlights contaminations of the industrial raw material.

The ^{13}C CPMAS NMR spectra (Fig. 4b) were recorded on the composites since they evidence the carbon atoms neighboring to hydrogen with an amplified intensity, thus, highlighting the organic compounds. The spectrum of CSP-D/28-500 MPa sample shows the typical resonances of the n-alkanes, associated with the first four carbon atoms in the chain (indicated as α, β, γ, δ in Fig. 4), while the chemical shifts are no longer resolvable from the fifth (ε) carbon atom on [66]. The paraffin resonances appear broader than usual due to the presence of graphite. Anyway, we can clearly notice that the δ resonance splits into three components. Fredi et al. proved that encapsulation of paraffin can

induce the formation of the so-called rotator phase, or also a non-uniform distribution of the conformational disorder to the γ-gauche effect near the chain ends, which causes, thereby, peak broadening [66]. The spectrum of CSP-D/55-500 MPa sample shows the same α,β,δ peaks belonging to the stearic/palmitic acid chains with slightly lower S/N, likely due to a lower amount of organic material in the composite and the possible interactions with graphite.

The ^{1}H NMR spectrum (Fig. 4c) of dolostone is characterized by a broad resonance centered at approximately 5 ppm and an extended sideband pattern due to incorporated molecular water, along with small peaks in the range of 2–0 ppm, attributed to hydroxide ions or mobile water [67]. After CSP, the water resonance shifts to 4.6 ppm, and the hydroxide peaks increase, suggesting the formation of some hydrated phases that are not clearly detectable by FTIR or XRD. This sharp resonance can be assigned to OH groups in hydrated crystal structures, aligning with the expected resonances in hydroxyapatite (HA) [61] that could form through the reaction between the phosphoric acid and dolostone in CSP.

The ^{1}H NMR spectra of the composites are dominated by the intense aliphatic proton signal at about 1 ppm, especially in CSP-D/28-500 MPa. The lower amount of organic phase in CSP-D/55-500 MPa leads to the detectable presence of both C-H and OH signals. The ^{31}P MAS NMR spectra (Fig. 4d) are characterized by an asymmetric resonance with a sharp component at about 0.7 ppm, with a major broad right shoulder at about 2.3 ppm and a minor left one at about −2 ppm (Fig. 4d). It is possible to attribute the main component to the bulk resonance of orthophosphates. Since the crystalline HA structure gives rise to a single P resonance centered at about 2.9 ppm [60,61], we can infer the presence, among others, of apatitic structure. The broadness of the band could be related to an amorphous calcium/magnesium phosphate phase or due to a distribution of ^{31}P isotropic chemical shifts associated with local disorder (inhomogeneous broadening). The nonstoichiometric apatite could stem from incorporation of a substantial amount of anionic (such as CO_3^{2-}) and cationic (Mg^{2+}) substitutions, as well as the presence of ion vacancies in the mineral structure. The sharp component at 0.7 ppm can likely be attributed to the relative sharpness of -HPOx groups on the surface or defective sites, and appears consistent with apatitic structures [61].

The cold-sintered materials possess fair mechanical strength, as evidenced in Fig. 5 by piston-on-three-ball bending tests. The mechanical properties generally increase with the CSP pressure; the only exception to this trend is represented by CSP-GR/55, peaking the strength at 400 MPa. While CSP-GR/28 samples were substantially denser than CSP-GR/55, the bending strength is comparable. On the other hand, the properties of pure dolostone, i.e., without the addition of any EGS-PCM, are substantially superior to those of the composites. In fact, CSP-D-500 MPa samples reached a strength of about 18 MPa, while the composite's properties are limited to 10–12 MPa.

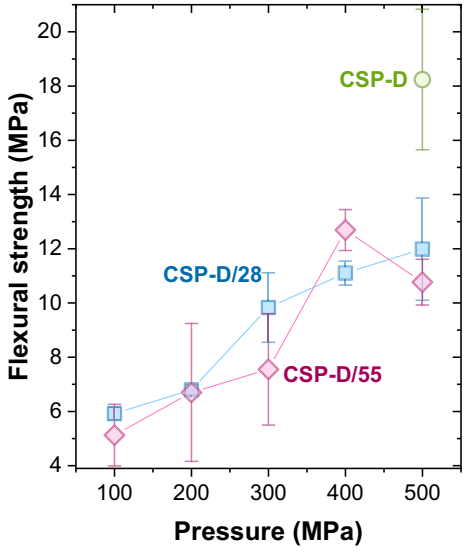

Fig. 5. Bending strength of cold-sintered dolostone and its composites obtained by the piston-on-three-ball method.

Fig. 6 presents the DSC curves obtained in heating, cooling, and reheating of the EGS-PCMs and on selected composites. The key features in terms of melting/crystallization enthalpy and peak temperature for the phase transitions are summarized in Table 1. We can clearly notice the typical signatures of the melting/crystallization events of the paraffin (Gr28) and organic acids blend (Gr55). These are also maintained in the dolostone-matrix composites with minimal shifts in the melting/crystallization temperatures. The latent heat (ΔH) values were determined by integrating the area under the peak relative to the baseline. Since the ΔH of the composites ($\Delta H_{D/EGS-PCM}$) originates from the PCM, the theoretical latent heat values can be calculated using the following equation[68]:

$$\Delta H_{D/EGS-PCM} = \eta \bullet \Delta H_{EGS-PCM} \quad (1)$$

where η is the actual mass fraction of the PCM in the composites and the $\Delta H_{EGS-PCM}$ represents the latent heat value of pure EGS-PCM. For the CSP-D/28 composites, the experimental ΔH values are close to the theoretical ones (i.e., ≈1/10 of the enthalpy of the pure EGS-PCM) with deviations of about 20% (or even lower) from the theoretical value. On the other hand, the CSP-D/55 material exhibited latent heat values about 25–44% lower than expected. This points out a deterioration of the Gr55 during processing with an estimated loss of about 25–44% of its mass. We can also notice the formation of some "irregular" and asymmetric features in the DSC plots of the cold sintering processed (CSPed) composites. This asymmetric feature is substantially lost in the composite containing Gr28 after a couple of heating/cooling cycles.

The effective ability of the PCM in changing the cooling/heating path of the material, stabilizing the temperature around the melting point, was evaluated on the dolostone-Gr28 composites (Fig. 7). Pure dolostone showed a regular heating and cooling profile with a nearly linear trend in the time-temperature plane. On the other hand, the composites deviate from the neat dolostone at around 25 °C, indicating the melting and crystallization of the PCM.

The stability of the composite was studied through a 8-days-long leakage test on the samples CSPed under 500 MPa. The results in Fig. 8a show a small weight loss on the first day, likely related to the evolution of adsorbed water, the weight remaining constant for the remaining days. The enthalpy of fusion was then measured on the CSP-D/28 composite (i.e., the one showing the best thermal performances according to the results in Table 1) after the leakage test, resulting in about 15.4 J g^{-1}. Cyclic tests (100 cycles) were operated to verify the stability of the material (Fig. 8b,c), confirming the absence of substantial loss in the thermal performances of the composite.

The thermophysical properties of the cold sintered materials depend on their composition and CSP pressure (Fig. 9, Table 2). The thermal diffusivity as well as the conductivity increase when increasing the CSP pressure due to the densification of the material. The two composites obtained under 500 MPa possess a fairly high thermal conductivity (about 1.9 W m^{-1} K^{-1}), which is substantially larger than that of pure cold-sintered dolostone (about 1.1 W m^{-1} K^{-1}) as a result of the graphite presence. Note that the drops in the composites' diffusivity can be attributed to the melting of the PCM (it matches the melting point of the two compounds). Indeed, due to the melting process, the specific heat, C_p, increases, thus causing a drop in the diffusivity, α, $\alpha = \lambda/\rho C_p$, with ρ and λ being the density and conductivity, respectivelly.

4. Discussion

The results show that CSP allows the consolidation of dolostone at

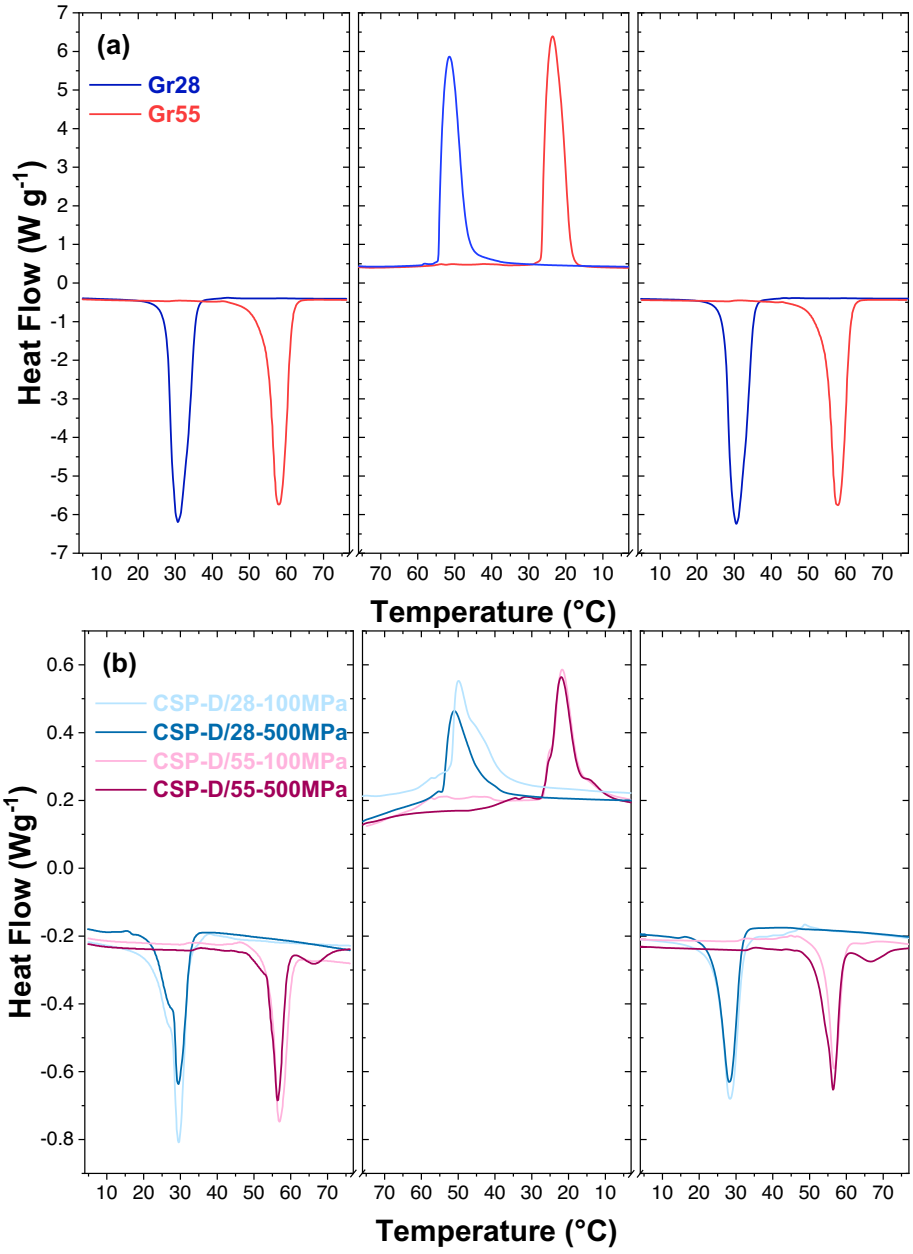

Fig. 6. DSC curves for Gr28, Gr55 PCM, and their composites in dolostone matrix, heating rate = 10 °C min^{-1} under N_2 flux.

Table 1
Thermal properties related to the melting and crystallization of the neat EGS_PCMs and their composites in the dolostone matrix. * total enthalpy including the second peak, first scan: 66.3 °C / 1.8 J g^{-1}; second scan: 66.6 °C / 1.8 J g^{-1}.

Sample	T_{m1}, °C	ΔH_{m1}, J g^{-1}	T_c, °C	ΔH_c, J g^{-1}	T_{m2}, °C	ΔH_{m2}, J g^{-1}
Gr28	30.7	191.3	23.5	191.0	30.5	191.9
CSP-D/28-100 MPa	29.0	16.8	21.6	15.6	28.5	16.2
CSP-D/28-500 MPa	29.5	14.4	21.9	14.2	28.1	14.1
Gr55	58.1	178.8	51.5	175.2	58.0	173.8
CSP-D/55-100 MPa	56.1	13.7	51.0	9.9	56.6	9.8
CSP-D/55-500 MPa	56.4	12.3 *	49.9	12.5	58.4	13.1*

room temperature through the dissolution of dolomite and the precipitation of various phosphates, as detected by NMR and FTIR. The microstructural analysis (Fig.3b) suggests that the particles mostly involved in the consolidation of the compound are the small submicrometric ones, which show clear densification and necking. These form a kind of matrix within which the bigger particles are accommodated. The sintering mechanism likely involves the dissolution of the dolostone that could occur on the external particles' surface or in the neck region (higher chemical potential induced by the external pressure, $\Delta\mu = \Omega\,\Delta p$, μ being the chemical potential, Ω the atomic volume and p the pressure) and the reprecipitation in the form of phosphates on the regions with negative pressure, i.e., the neck surface where the local pressure is negative. In fact, the curvature, κ, of the liquid meniscus on the neck surface is negative [13], thus inducing a negative pressure $\Delta p = \gamma k$, γ being the surface tension of the solution. We note that the dissolution from the particle center (densifying the ceramic) is accelerated when increasing the external pressure, while the rate by which mass is removed from the external particle surface is independent of the applied

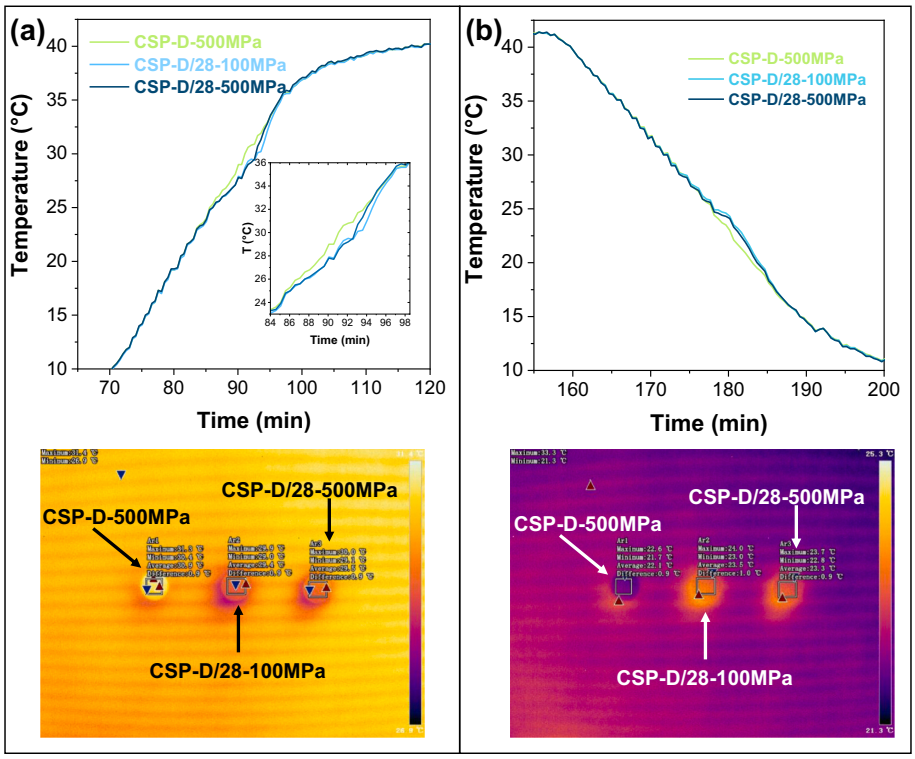

Fig. 7. (a) Heating and (b) cooling profiles of dolostone and dolostone-matrix composites (including Gr28 compound) obtained in a climatic chamber under heating and cooling rates of 1°C min^{-1}. The IR thermocamera images highlight a clear temperature difference between the neat dolostone and the composite samples.

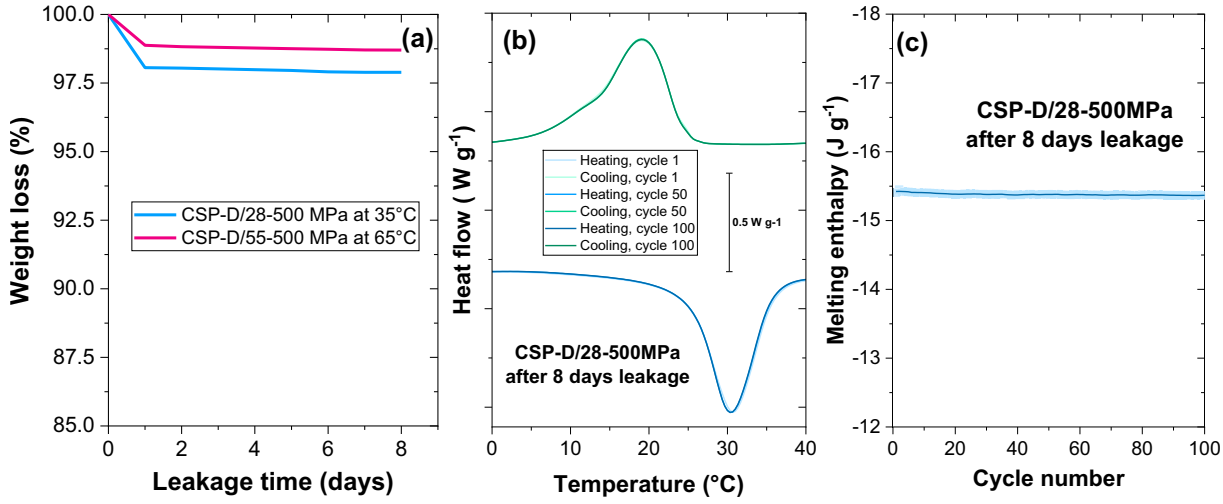

Fig. 8. (a) Weight loss during the leakage test (note that the PCM weight is about 10 wt% of the composite). (b) Cyclic DSC curves on the CSP-D/28-500 MPa sample after the leakage test (the curves can be poorly distinguished as they fully overlaps), (c) melting enthalpy evolution with cycling number.

pressure (non-densifying transport). In this context, an increase in the external pressure promotes a shift from the non-densifying to the densifying transport mechanism responsible for the density increase in Fig.2a.

More importantly, CSP enables the consolidation of ceramic-matrix composites containing a thermolabile phase change material for thermal energy storage at near room temperature. The presence of the PCMs after CSP is confirmed by NMR, FTIR, and XRD (Figs. 3,4); the thermal energy storage ability is verified by DSC (Fig. 6) and by the temperature profiles measured in heating/cooling cycles (Fig. 7). The effect of the PCM in stabilizing the temperature is detectable, even if the samples were relatively small (60 mg of EGS-PCM in 540 mg of dolostone) with a large surface-to-volume ratio.

The thermal conductivity of the composites is relatively high (≈1.9 W m^{-1} K^{-1}) and substantially superior to that of cold-sintered dolostone (≈1.1 W m^{-1} K^{-1}). This points out the crucial role of the graphite addition, which not only stabilizes the PCM but also increases the thermal conductivity of the composite, thus facilitating the heat exchange with the environment and increasing the efficiency of the thermal energy storage process.

The overall mechanical properties of the PCM-containing composites are indeed lower than those of neat CSP-dolostone (Fig. 5), as the polymer-containing regions act as large defects within the ceramic matrix. Although the PCM incorporation causes a decrease in the bending strength from about 18 to about 10–12 MPa (CSP under 500 MPa), the mechanical properties of the composites are still fairly good

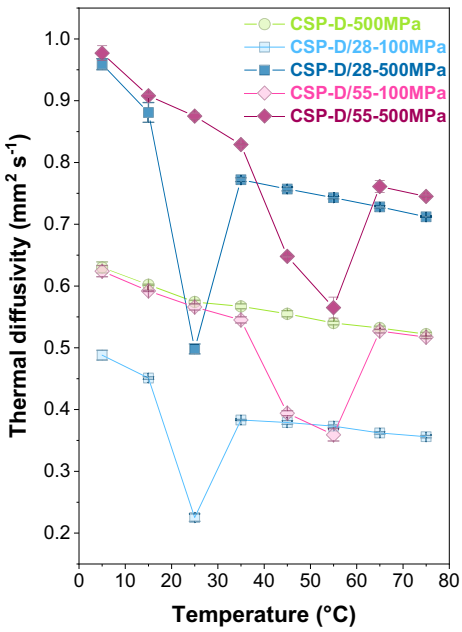

Fig. 9. Thermal diffusivity obtained by the LFA method at different temperatures on composites and neat dolostone consolidated by CSP. The clear drop in the thermal diffusivity of the composites can be detected close to the melting point of the PCM.

Table 2
Thermal and physical properties of the cold sintered materials at 15 °C.

Sample	Thermal diffusivity ($mm^2\ s^{-1}$)	Specific heat capacity ($J\ g^{-1}{\cdot}K^{-1}$)	Thermal conductivity ($W\ m^{-1}{\cdot}K^{-1}$)
CSP-D-500 MPa	0.602 ± 0.001	0.91 ± 0.01	1.166 ± 0.003
CSP-D/28-100 MPa	0.451 ± 0.002	1.04 ± 0.02	1.110 ± 0.009
CSP-D/28-500 MPa	0.881 ± 0.016	1.05 ± 0.03	1.950 ± 0.040
CSP-D/55-100 MPa	0.592 ± 0.001	0.99 ± 0.01	0.997 ± 0.002
CSP-D/55-500 MPa	0.908 ± 0.003	1.03 ± 0.01	1.865 ± 0.005

and acceptable for non-load-bearing applications. As an example, our CSPed composites possess mechanical properties largely surpassing those of plaster and plaster-matrix composites [69–71]. Indeed, the bending strength generally increases with the CSP pressure, mimicking the density evolution (Fig. 2a). However, the CSP-GR/55 sample strength peaks at 400 MPa; higher pressure slightly decreases the mechanical properties. This could be tentatively attributed to the formation of defects (delamination, microcracking) that are often observed in pressed artifacts under high pressure (these originate from the pressure gradients inside the material or the spring back during the extraction from the mold).

The relative density of the composites obtained by CSP appears generally larger than that of the net dolostone (Fig. 2a). This is an artifact related to the fact that the porosity is "confined" in the dolostone matrix, while the "PCM islands" are fully dense. Indeed, the pressure application in CSP modifies the shape of the EGS-PCM, which gets flattened orthogonally to the external load application (Fig. 2c,d).

A critical point appears to be the choice of the right type of PCM. Surprisingly, the PCM possessing the lower melting point (Gr28, paraffin) is less affected by the CSP process. This is confirmed by the fact that the melting/crystallization enthalpy of the D/28 composites is close to the theoretical value calculated from the composition of the composite (i.e., 10 wt% of EGS-PCM in dolostone). On the other hand, the materials containing Gr55 compounds lose about half of their thermal energy storage ability during the processing, compared to the theoretical value. The deterioration or the loss of the Gr55 compound is confirmed by the FTIR and NMR, while the low amount of crystalline PCM at room temperature is proven by XRD. This can likely be attributed to the presence of hydrophilic units (carboxylic acid) in the stearic/palmitic acid mixture of Gr55, which can interact with the water solution in CSP and be eventually extracted from the stabilizer (i.e, the graphite). The dispersion of PCM in the CSP solution for the Gr55 compound is likely related to the lower density level of the D/55 composites and to their heterogeneous microstructures (Fig. 2a, f-m), where the PCM and graphite dispersion poison the CSP consolidation. Actually, we can clearly detect in D/55 composites large regions that are substantially not consolidated under low pressure (Figs. 2f, g, h**).** These eventually collapse under larger pressure in "dark contrast" areas **(**Figs. 2i, l, m**),** where the dolomite grains are covered by graphite and organics.

Finally, the formation of asymmetric shapes in the DSC peak (Fig. 6) in the composites could be attributed to a change in the confinement conditions of the PCM [66](e.g., a change in the distance between graphite lamellas) or to a demixing between stearic/palmitic acids in the Gr55-containing compound. The modification in the confinement conditions is likely dominant for the composite including Gr28 PCM. In fact, after a couple of melting tests, the shape returns to its original one. Indeed, when the PCM is liquid, the graphite lamellas can slightly rearrange, getting closer to the pre-CSP conditions. On the other hand, the peak asymmetry or even splitting into two clear components seems irreversible for Gr55, suggesting that it can actually originate from a phase separation in the PCM.

The leakage test shows a modest weight loss located in the first day of the test (Fig. 8a). The weight loss is about 1–2 wt%, much lower than the PCM content, and can likely be attributed to the adsorbed humidity. The absence of PCM loss is confirmed by the DSC after the leakage test, showing the same enthalpy values of the untreated material (about 15.4 $J\ g^{-1}$). Therefore, no deterioration of the thermal properties occurred during the 8-days holding above the melting point of the PCM. Cyclic DSC (Fig. 8b,c) confirms the stability of the composite.

The overall thermal energy storage performance (about 15 $J\ g^{-1}$) is interesting but indeed much smaller than what can be achieved by incorporating a large amount of PCMs in lightweight matrices, such as polymers. PCMs have already been introduced in inorganic matrices like concrete [45,46], geopolymers [44,47–50], or plasters [42,43] with success. The thermal energy storage of these composites is generally comparable with the one obtained in this work, the literature data mainly ranging between 3 and 24 $J\ g^{-1}$. A general drawback of the standard approaches studied in this context is the abundant use of micro- or nano-encapsulated PCM to avoid its leakage or separation from the inorganic matrix during the setting. A clear advantage of the CSP approach is the successful production of an inorganic matrix without the need for encapsulation. While not being the first achievement of such a goal [43,44], it is still not trivial. Higher thermal energy performances have been reported in some composites (even above 100 $J\ g^{-1}$); however, those studies used encapsulated PCM, and no data about the mechanical properties are available [42]. In this context, our results provide a first proof of concept of a new approach based on sintering to incorporate PCMs inside an inorganic matrix, which is radically different from the discussed literature based on matrices obtained by hardening (setting).

These results pave the way to a new avenue to obtain materials with low embodied energy and CO_2, processed at room temperature, possessing fair mechanical and thermal properties, and the ability to store thermal energy. The material developed herein could find application in panels or other non-load-bearing masonry, with possible competition with plaster or bricks. It is, for instance, not trivial to notice that the mechanical properties measured herein are substantially competitive

with those of fired bricks [72–74]. The room temperature processing developed herein is also attractive in simplifying the CSP setup, thus facilitating a possible scale-up of the technology. Scale-up challenges still remain in terms of productivity that can be significantly lower than that achieved by extrusion technologies used in the brick (and partially tile) industry.

5. Conclusions

The cold sintering process enables the room temperature consolidation of milled dolostone powders through its partial dissolution and precipitation in the form of phosphate phases. The process allows the incorporation of thermolabile materials, like low molecular weight polymers or other organic compounds, within a stiff and strong ceramic matrix. Specifically, we showed that this approach allows the manufacturing of dolostone-matrix composites containing polymer phases for thermal energy storage at near room temperature.

The obtained CSPed composites possess fair mechanical properties, relatively good thermal conductivity, and an ability to store thermal energy through the latent heat of fusion/crystallization of an organic compound up to about 15 J g^{-1}. The results also point out that a critical issue is the correct choice of the phase change material due to its possible interaction with the cold sintering solution.

The developed process represents a promising pathway toward the design of innovative and sustainable materials that can transform the future of the construction sector.

CRediT authorship contribution statement

Dovilė Škarnulytė: Writing – original draft, Methodology, Investigation. **Levent Karacasulu:** Writing – review & editing, Validation, Supervision, Investigation. **Emanuela Callone:** Writing – original draft, Methodology, Investigation. **Sereno Sacchet:** Methodology, Investigation. **Luca Fambri:** Writing – review & editing, Supervision, Resources. **Meriem Bembli:** Investigation. **Mauro Bortolotti:** Software, Investigation. **Paolo Bettotti:** Investigation. **Jonathan Selorm Degbedzui:** Investigation. **Giulia Fredi:** Writing – review & editing, Resources, Methodology, Conceptualization, Investigation. **Sandra Dirè:** Writing – original draft, Supervision, Resources, Methodology, Conceptualization. **Mattia Biesuz:** Writing – original draft, Visualization, Validation, Resources, Project administration, Methodology, Conceptualization.

Declaration of competing interest

The authors declare that they have no known competing financial interests or personal relationships that could have appeared to influence the work reported in this paper.

Acknowledgments

The company Miniera San Romedio srl (Italy) is warmly acknowledged for the support and for the precious collaboration. This work was funded by “Fondazione VRT” within the project “Cold sintering di compositi ceramico-polimero per lo stoccaggio di energia termica”; all the authors warmly acknowledge the financial contributions. Meriem Bembli acknowledges the support from the overhead of the project Space It Up and received funding from the ASI and the MUR—Contract no. 2024-5-E.0-CUP no. I53D24000060005.

Data availability

Data will be made available on request.

References

[1] A. Mollaei, B. Byers, C. Christovan, A. Olumo, C. De Wolf, C. Bachmann, C. Haas, A global perspective on building material recovery incorporating the impact of regional factors, J. Clean. Prod. 429 (2023) 139525, https://doi.org/10.1016/j.jclepro.2023.139525.
[2] https://www.eea.europa.eu/en/topics/in-depth/buildings-and-construction, 2026.
[3] J. Dsilva, S. Zarmukhambetova, J. Locke, Assessment of building materials in the construction sector: a case study using life cycle assessment approach to achieve the circular economy, Heliyon 9 (2023) e20404, https://doi.org/10.1016/j.heliyon.2023.e20404.
[4] M.N. Rahaman, Ceramic Processing and Sintering, Marcel Dekker, New York, USA, 1996.
[5] M. Biesuz, S. Grasso, V.M. Sglavo, What’s new in ceramics sintering? A short report on the latest trends and future prospects, Curr. Opin. Solid State Mater. Sci. 24 (2020) 100868, https://doi.org/10.1016/j.cossms.2020.100868.
[6] E.A. Olevsky, D.V. Dudina, Field- Assisted Sintering, 2026.
[7] S. Grasso, Y. Sakka, G. Maizza, Electric current activated/assisted sintering (ECAS): a review of patents 1906–2008, Sci. Technol. Adv. Mater. 10 (2009) 053001.
[8] J. Guo, R. Floyd, S. Lowum, J.-P. Maria, T. Herisson de Beauvoir, J.-H. Seo, C. A. Randall, Cold sintering: progress, challenges, and future opportunities, Annu. Rev. Mater. Res. 49 (2019) 275–295, https://doi.org/10.1146/annurev-matsci-070218-010041.
[9] S. Grasso, M. Biesuz, L. Zoli, G. Taveri, A.I. Duff, D. Ke, A. Jiang, M.J. Reece, A review of cold sintering processes, Adv. Appl. Ceram. 119 (2020) 115–143, https://doi.org/10.1080/17436753.2019.1706825.
[10] C. Vakifahmetoglu, L. Karacasulu, Cold sintering of ceramics and glasses: a review, Curr. Opin. Solid State Mater. Sci. 24 (2020) 100807, https://doi.org/10.1016/j.cossms.2020.100807.
[11] A. Galotta, V.M. Sglavo, The cold sintering process: a review on processing features, densification mechanisms and perspectives, J. Eur. Ceram. Soc. 41 (2021) 1–17, https://doi.org/10.1016/j.jeurceramsoc.2021.09.024.
[12] A. Ndayishimiye, M.Y. Sengul, S.H. Bang, K. Tsuji, K. Takashima, T. Hérisson de Beauvoir, D. Denux, J.-M. Thibaud, A.C.T. van Duin, C. Elissalde, G. Goglio, C. A. Randall, Comparing hydrothermal sintering and cold sintering process: mechanisms, microstructure, kinetics and chemistry, J. Eur. Ceram. Soc. 40 (2020) 1312–1324, https://doi.org/10.1016/j.jeurceramsoc.2019.11.049.
[13] M. Biesuz, G. Taveri, A.I. Duff, E. Olevsky, D. Zhu, C. Hu, S. Grasso, A theoretical analysis of cold sintering, Adv. Appl. Ceram. 119 (2020) 75–89, https://doi.org/10.1080/17436753.2019.1692173.
[14] J. Gonzalez-Julian, K. Neuhaus, M. Bernemann, J. Pereira da Silva, A. Laptev, M. Bram, O. Guillon, Unveiling the mechanisms of cold sintering of ZnO at 250°C by varying applied stress and characterizing grain boundaries by kelvin probe force microscopy, Acta Mater. 144 (2018) 116–128, https://doi.org/10.1016/j.actamat.2017.10.055.
[15] D. Wang, K. Tsuji, C.A. Randall, S. Trolier-McKinstry, Model for the cold sintering of lead zirconate titanate ceramic composites, J. Am. Ceram. Soc. 103 (2020) 4894–4902, https://doi.org/10.1111/jace.17269.
[16] J. Guo, H. Guo, A.L. Baker, M.T. Lanagan, E.R. Kupp, G.L. Messing, C.A. Randall, Cold sintering: a paradigm shift for processing and integration of ceramics, Angew. Chem. Int. Ed. 55 (2016) 11457–11461, https://doi.org/10.1002/anie.201605443.
[17] A. Galotta, F. Agostinacchio, A. Motta, S. Dirè, V.M. Sglavo, Mechanochemical synthesis and cold sintering of mussel shell-derived hydroxyapatite nano-powders for bone tissue regeneration, J. Eur. Ceram. Soc. 43 (2023) 639–647, https://doi.org/10.1016/j.jeurceramsoc.2022.09.024.
[18] D. Beauvoir, S. Dursun, L. Gao, C. Randall, New opportunities in metallization integration in cofired electroceramic multilayers by the cold sintering process, ACS Appl. Electron. Mater. 1 (2019) 1198–1207, https://doi.org/10.1021/acsaelm.9b00184.
[19] S. Funahashi, H. Guo, J. Guo, A.L. Baker, K. Wang, K. Shiratsuyu, C.A. Randall, Cold sintering and co-firing of a multilayer device with thermoelectric materials, J. Am. Ceram. Soc. 100 (2017) 3488–3496, https://doi.org/10.1111/jace.14852.
[20] S.H. Bang, T.H. De Beauvoir, C.A. Randall, Densification of thermodynamically unstable tin monoxide using cold sintering process, J. Eur. Ceram. Soc. 39 (2019) 1230–1236, https://doi.org/10.1016/j.jeurceramsoc.2018.11.026.
[21] M. Luginina, R. Orru, G. Cao, D. Grossin, F. Brouillet, G. Chevallier, C. Thouron, C. Drouet, First successful stabilization of consolidated amorphous calcium phosphate (ACP) by cold sintering: toward highly-resorbable reactive bioceramics, J. Mater. Chem. B 8 (2020) 629–635, https://doi.org/10.1039/C9TB02121C.
[22] H.-J. Kim, T.-H. Kim, J.-M. Oh, F. Salles, G. Chevallier, C. Thouron, P. Trens, J. Soulie, S. Cazalbou, C. Drouet, Cold sintering yields first layered double hydroxides (LDH) monolithic materials, Mater. Sci. Eng. B 280 (2022) 115704, https://doi.org/10.1016/j.mseb.2022.115704.
[23] N. Guo, H.-Z. Shen, P. Shen, One-step synthesis and densification of BaTiO3 by reactive cold sintering, Scr. Mater. 213 (2022) 114628, https://doi.org/10.1016/j.scriptamat.2022.114628.
[24] J.P. Ma, X.M. Chen, W.Q. Ouyang, J. Wang, H. Li, J.L. Fang, Microstructure, dielectric, and energy storage properties of BaTiO3ceramics prepared via cold sintering, Ceram. Int. 44 (2018) 4436–4441, https://doi.org/10.1016/j.ceramint.2017.12.044.
[25] J. Gao, Z. Xia, Q. Ding, Y. Liu, P. Yan, Y. Hu, L. Wang, W. Luo, Y. Fan, W. Jiang, Cold sintering of highly transparent calcium fluoride nanoceramic as a universal platform for high-power lighting, Adv. Funct. Mater. 33 (2023), https://doi.org/10.1002/adfm.202302088.

[26] J. Gao, Y. Ren, Q. Ding, P. Yan, Y. Liu, Y. Hu, J. Chen, Z. Cheng, Y. Fan, W. Jiang, Cold sintering of CsPbBr3 quantum dots embedded KBr ceramics for LED displays, J. Mater. 11 (2025) 100933, https://doi.org/10.1016/j.jmat.2024.100933.
[27] P. Yan, M. Si, Y. Liu, Y. Ren, Q. Ding, W. Jiang, Y. Fan, W. Jiang, Large internal stress induced nonlinear current-voltage behavior in nanodiamond strengthened ZnO ceramics, Nat. Commun. 15 (2024) 9812, https://doi.org/10.1038/s41467-024-54279-x.
[28] S. Marín-Cortés, M. Biesuz, A. Serrano, E. De Bona, E. Enríquez, J.F. Fernández, V. M. Sglavo, Promoting the circularity of ceramic materials through cold sintering of aggregates from construction and demolition waste, Open Ceram. 20 (2024) 100692, https://doi.org/10.1016/j.oceram.2024.100692.
[29] I. Maruyama, N.K. Bui, A. Meawad, R. Kurihara, Y. Mitani, H. Hyodo, M. Kanematsu, T. Noguchi, Cold-sintered carbonated concrete waste fines: a calcium carbonate concrete block, J. Adv. Concr. Technol. 22 (2024) 406–418, https://doi.org/10.3151/jact.22.406.
[30] S. Marín-Cortés, A. Serrano, E. Enríquez, J.F. Fernández, Dense ceramics by cold reaction sintering using 95% powdered construction and demolition waste and sodium silicate, Constr. Build. Mater. 451 (2024) 138917, https://doi.org/10.1016/j.conbuildmat.2024.138917.
[31] A. Galotta, E. Giust, M. Bortolotti, G.D. Sorarù, V.M. Sglavo, M. Biesuz, Cold sintering of diatomaceous earth, J. Am. Ceram. Soc. (2021), https://doi.org/10.1111/jace.17863. IN PRESS.
[32] E. Kamseu, M. Biesuz, A.-T. Akono, J.N.N. Fokoua, E. De Bona, N. Buettner, H. Lee, C. Leonelli, S. Rossignol, V.M. Sglavo, Cold-sintered laterite-based geopolymers: densification, microstructure and micromechanics, J. Eur. Ceram. Soc. 44 (2024) 116798, https://doi.org/10.1016/j.jeurceramsoc.2024.116798.
[33] L. Lattanzi, A. Conte, A. Sin, J.M. Garcia, C.A. Randall, P. Colombo, Cold sintering of geopolymer powders, J. Am. Ceram. Soc. (2024), https://doi.org/10.1111/jace.20331.
[34] K. Nishikawa, S. Hashimoto, H. Imai, S. Rossignol, Cold reaction sintering for preparation of ultra-dense geopolymer products, Constr. Build. Mater. 328 (2022) 127101, https://doi.org/10.1016/j.conbuildmat.2022.127101.
[35] O.A. Radwan, M.A. Hussein, R.A. Assaggaf, J.D. Humphrey, M. Al-Hashem, A. A. Mahmoud, Rebuilding with sand roses: cold sintering of sand-gypsum mixture for sustainable brick production, Constr. Build. Mater. 442 (2024) 137642, https://doi.org/10.1016/j.conbuildmat.2024.137642.
[36] O.A. Radwan, M.A. Hussein, R. Assaggaf, J.D. Humphrey, A. Abdelaal, Cold sintering of sand-evaporite mixtures for sustainable brick applications in hot, arid climates: a laboratory upscaling study, Constr. Build. Mater. 492 (2025) 142981, https://doi.org/10.1016/j.conbuildmat.2025.142981.
[37] K. Pielichowska, K. Pielichowski, Phase change materials for thermal energy storage, Prog. Mater. Sci. 65 (2014) 67–123, https://doi.org/10.1016/j.pmatsci.2014.03.005.
[38] A. de Gracia, L.F. Cabeza, Phase change materials and thermal energy storage for buildings, Energ. Buildings 103 (2015) 414–419, https://doi.org/10.1016/j.enbuild.2015.06.007.
[39] Q. Al-Yasiri, M. Alktranee, M. Szabó, Metal fibers-enhanced PCM thermal energy storage unit: an experimental approach on a composite roof application, Int. J. Thermofluids 23 (2024) 100812, https://doi.org/10.1016/j.ijft.2024.100812.
[40] O. Gencel, G. Hekimoglu, A. Sarı, A. Ustaoglu, S. Subasi, M. Marasli, E. Erdogmus, S.A. Memon, Glass fiber reinforced gypsum composites with microencapsulated PCM as novel building thermal energy storage material, Constr. Build. Mater. 340 (2022) 127788, https://doi.org/10.1016/j.conbuildmat.2022.127788.
[41] X. Zuo, Q. Li, Y. Tang, Y. Li, X. Zhao, H. Yang, Experimental and numerical investigation of building envelopes constructed with mineral based composite phase change material for thermal management, Constr. Build. Mater. 474 (2025) 141067, https://doi.org/10.1016/j.conbuildmat.2025.141067.
[42] B. Maleki, A. Khadang, H. Maddah, M. Alizadeh, A. Kazemian, H.M. Ali, Development and thermal performance of nanoencapsulated PCM/ plaster wallboard for thermal energy storage in buildings, J. Build. Eng. 32 (2020) 101727, https://doi.org/10.1016/j.jobe.2020.101727.
[43] A. Karaipekli, A. Sarı, Development and thermal performance of pumice/organic PCM/gypsum composite plasters for thermal energy storage in buildings, Sol. Energy Mater. Sol. Cells 149 (2016) 19–28, https://doi.org/10.1016/j.solmat.2015.12.034.
[44] A. Przybek, Geopolymer foams loaded with diatomite/paraffin granules for enhanced thermal energy storage, Materials 18 (2025) 4512, https://doi.org/10.3390/ma18194512.
[45] S.J. Osibodu, A.M. Adeyinka, O.V. Mbelu, Phase change material integration in concrete for thermal energy storage: techniques and applications in sustainable building, Sustain. Energy Res. 11 (2024) 45, https://doi.org/10.1186/s40807-024-00138-8.
[46] O.H. Ören, E. Mandev, M. Kaya, A. Sarı, G. Hekimoğlu, İ.Ü. Çıkman, S. Subaşı, M. Maraşlı, O. Gencel, Effects of microencapsulated phase change material on physico-mechanical and thermoregulation performance of lightweight geopolymer concrete with zeolite and perlite, J. Energy Storage 109 (2025) 115225, https://doi.org/10.1016/j.est.2024.115225.
[47] B. El Moustapha, S. Bonnet, A. Khelidj, N. Leklou, D. Froelich, I.A. Babah, C. Charbuillet, A. Khalifa, Compensation of the negative effects of micro-encapsulated phase change materials by incorporating metakaolin in geopolymers based on blast furnace slag, Constr. Build. Mater. 314 (2022) 125556, https://doi.org/10.1016/j.conbuildmat.2021.125556.
[48] A. Bąk, K. Pławecka, P. Bazan, M. Łach, Influence of the addition of phase change materials on thermal insulation properties of foamed geopolymer structures based on fly ash, Energy 278 (2023) 127624, https://doi.org/10.1016/j.energy.2023.127624.
[49] A. El Majd, S. Sair, H. Ait Ousaleh, K. Moulakhnif, Z. Moujoud, I. Belrhazi, N. Belouaggadia, A. El Bouari, Enhancing heat storage in geopolymer foams via shape-stabilized phase change materials: a comparative analysis of foaming techniques, J. Build. Eng. 112 (2025) 113799, https://doi.org/10.1016/j.jobe.2025.113799.
[50] Y. Fang, M.R. Ahmad, J.-C. Lao, L.-P. Qian, J.-G. Dai, Development of artificial geopolymer aggregates with thermal energy storage capacity, Cem. Concr. Compos. 135 (2023) 104834, https://doi.org/10.1016/j.cemconcomp.2022.104834.
[51] C.M. Belfiore, S. Parisi, S. Menta, P. Mazzoleni, Use of volcanic ash and chamotte as substitute temper in the production of ceramic tiles, Appl. Clay Sci. 262 (2024) 107603, https://doi.org/10.1016/j.clay.2024.107603.
[52] Z. Guo, J. Qiao, X. Liu, F. Lin, M. Liu, M. Fang, Z. Huang, X. Zhang, X. Min, Advances in mineral-based composite phase change materials for energy storage: a review, green and smart, Min. Eng. 1 (2024) 447–473, https://doi.org/10.1016/j.gsme.2024.11.005.
[53] D. Li, X. Zuo, X. Zhang, Y. Tang, X. Zhao, Y. Zhang, H. Yang, Emerging urchin-like core-shell mineral microspheres with efficient photothermal conversion and solar energy storage, J. Energy Storage 68 (2023) 107661, https://doi.org/10.1016/j.est.2023.107661.
[54] A. Palacios, M.E. Navarro-Rivero, B. Zou, Z. Jiang, M.T. Harrison, Y. Ding, A perspective on phase change material encapsulation: guidance for encapsulation design methodology from low to high-temperature thermal energy storage applications, J. Energy Storage 72 (2023) 108597, https://doi.org/10.1016/j.est.2023.108597.
[55] S. Sacchet, F. Valentini, A. Benin, M. Guidolin, R. Po, L. Fambri, Expanded graphite (EG) stabilization of stearic and palmitic acid mixture for thermal Management of Photovoltaic Cells, C — J. Carbon Res. 10 (2024) 46, https://doi.org/10.3390/c10020046.
[56] D.K. Shetty, A.R. Rosenfield, P. McGuire, G.K. Bansal, W.H. Duckworth, Biaxial flexure test for ceramics, Am. Ceram. Soc. Bull. 59 (1980) 1193. American Ceramic Society Bulletin this journal doesn't have a profile on ResearchGate yet. Interested in this journal? Get notified when it activates its profile, and start getting updates.
[57] Y. Maor, M.B. Toffolo, Y. Feldman, J. Vardi, H. Khalaily, Y. Asscher, Dolomite in archaeological plaster: an FTIR study of the plaster floors at Neolithic Motza, Israel, J. Archaeol. Sci. Rep. 48 (2023) 103862, https://doi.org/10.1016/j.jasrep.2023.103862.
[58] D. Varshney, M. Ahmadi, M.J.-F. Guinel, B.R. Weiner, G. Morell, Single-step route to diamond-nanotube composite, Nanoscale Res. Lett. 7 (2012) 535, https://doi.org/10.1186/1556-276X-7-535.
[59] Z. Hajdari, H.O. Ćurković, V. Čadež, S. Šegota, Corrosion protection of cupronickel alloy by self-assembled films of fatty acids, J. Electrochem. Soc. 163 (2016) C145–C155, https://doi.org/10.1149/2.0321605jes.
[60] F. Munarin, P. Petrini, R. Gentilini, R.S. Pillai, S. Dirè, M.C. Tanzi, V.M. Sglavo, Micro- and nano-hydroxyapatite as active reinforcement for soft biocomposites, Int. J. Biol. Macromol. 72 (2015) 199–209, https://doi.org/10.1016/j.ijbiomac.2014.07.050.
[61] M. Frasnelli, F. Cristofaro, V.M. Sglavo, S. Dirè, E. Callone, R. Ceccato, G. Bruni, A. I. Cornaglia, L. Visai, Synthesis and characterization of strontium-substituted hydroxyapatite nanoparticles for bone regeneration, Mater. Sci. Eng. C 71 (2017) 653–662, https://doi.org/10.1016/j.msec.2016.10.047.
[62] Md. Sahadat Hossain, S. Ahmed, FTIR spectrum analysis to predict the crystalline and amorphous phases of hydroxyapatite: a comparison of vibrational motion to reflection, RSC Adv. 13 (2023) 14625–14630, https://doi.org/10.1039/D3RA02580B.
[63] I. Pianet, A. Gutiérrez Garcia-Moreno, M.-C. Savin, N. Frerebeau, J. Trebosc, P. Florian, M.P. Lapuente Mercadal, 13C, 25Mg, and 43Ca solid-state NMR for the purpose of dolomitic marbles provenance elucidation, Materials 16 (2023) 1468, https://doi.org/10.3390/ma16041468.
[64] J.K. Moore, J.A. Surface, A. Brenner, P. Skemer, M.S. Conradi, S.E. Hayes, Quantitative identification of metastable magnesium carbonate minerals by solid-state ^{13}C NMR spectroscopy, Environ. Sci. Technol. 49 (2015) 657–664, https://doi.org/10.1021/es503390d.
[65] A. Gutiérrez Garcia-M, M.C. Savin, N. Cantin, S. Boudoumi, P. Lapuente, R. Chapoulie, I. Pianet, NMR as a new tool for cultural heritage application: the provenance of ancient white marbles, Archaeometry 61 (2019) 795–808, https://doi.org/10.1111/arcm.12456.
[66] G. Fredi, S. Dirè, E. Callone, R. Ceccato, F. Mondadori, A. Pegoretti, Docosane-Organosilica microcapsules for structural composites with thermal energy storage/release capability, Materials 12 (2019) 1286, https://doi.org/10.3390/ma12081286.
[67] H. Nebel, M. Neumann, C. Mayer, M. Epple, On the structure of amorphous calcium carbonate—a detailed study by solid-state NMR spectroscopy, Inorg. Chem. 47 (2008) 7874–7879, https://doi.org/10.1021/ic8007409.
[68] W. Jia, C. Wang, T. Wang, Z. Cai, K. Chen, Preparation and performances of palmitic acid/diatomite form-stable composite phase change materials, Int. J. Energy Res. 44 (2020) 4298–4308.
[69] M. Keppert, V. Pommer, K. Šádková, A. Botnari, E. Vejmelková, D. Koňáková, Blended lime plasters with biomass ash and natural fibres reinforcement, J. Phys. Conf. Ser. 2792 (2024) 012004, https://doi.org/10.1088/1742-6596/2792/1/012004.
[70] L.M.S. Jara, J.A.F. Yepes, J.J.P. Pérez, Analysis of the resistance to bending of gypsum with added graphene, Coatings 11 (2021) 650, https://doi.org/10.3390/coatings11060650.

[71] V. Claude, S. Charron, F. de Barquin, I. Dirkx, Microencapsulated phase changing materials for gypsum plasters: a practical approach, Constr. Mater. 1 (2021) 188–202, https://doi.org/10.3390/constrmater1030012.
[72] S. Karaman, E. Sabit, G. Hikmet, Firing temperature and firing time influence on mechanical and physical properties of clay bricks, J. Sci. Ind. Res. (India). 65 (2006) 153–159.
[73] J. Cai, N. Lv, X. Jia, R. Zhang, G. Xu, L. Cai, Q. Tian, Properties of permeable ceramic brick prepared with felsite tailing, J. Build. Eng. 44 (2021) 103426, https://doi.org/10.1016/j.jobe.2021.103426.
[74] C.L. Cramer, E. Lara-Curzio, A.M. Elliott, T.G. Aguirre, B. Yoon, B.A. Fricke, V. Rao, P. Jain, K. Nawaz, Material selection and manufacturing for high-temperature heat exchangers: review of state-of-the-art development, opportunities, and challenges, Int. J. Ceram. Eng. Sci. 6 (2024), https://doi.org/10.1002/ces2.10230.